MNRAS **472,** 2633–2642 (2017) doi:10.1093/mnras/stx2081

Dynamical history of a binary cluster: Abell 3653

Turgay Caglar[1] and Murat Hudaverdi[1,2]★

[1]*Yıldız Technical University, Faculty of Science and Art, Department of Physics, Istanbul 34220, Turkey*
[2]*AUM, College of Engineering and Technology, Department of Science, Dasman 15453, Kuwait*

Accepted 2017 August 10. Received 2017 August 10; in original form 2017 January 13

ABSTRACT

We study the dynamical structure of a bimodal galaxy cluster Abell 3653 at $z = 0.1089$ using optical and X-ray data. Observations include archival data from the Anglo-Australian Telescope, X-ray observatories *XMM–Newton* and *Chandra*. We draw a global picture for A3653 using galaxy density, X-ray luminosity and temperature maps. The galaxy distribution has a regular morphological shape at the 3 Mpc size. The galaxy density map shows an elongation in the east–west direction, which perfectly aligns with the extended diffuse X-ray emission. We detect two dominant groups around the two brightest cluster galaxies (BCGs). BCG1 ($z = 0.1099$) can be associated with the main cluster A3653E, and a foreground subcluster A3653W is concentrated at BCG2 ($z = 0.1075$). Both X-ray peaks are dislocated from the BCGs by ∼35 kpc, which suggest an ongoing merger process. We measure the subcluster gas temperatures of 4.67 and 3.66 keV, respectively. Two-body dynamical analysis shows that A3653E and A3653W are very likely gravitationally bound (93.5 per cent probability). The highly favoured scenario suggests that the two subclusters have a mass ratio of 1.4 and are colliding close to the plane of sky ($\alpha = 17.61^{\circ}$) at 2400 km s^{-1}, and will undergo core passage in 380 Myr. The temperature map also significantly shows a shock-heated gas (6.16 keV) between the subclusters, which confirms the supersonic infalling scenario.

Key words: galaxies: clusters: individual: Abell 3653 – galaxies: clusters: intracluster medium – X-rays: galaxies: clusters.

1 INTRODUCTION

Cosmological models predict that small structures form first then progressively merge into larger structures. Clusters of galaxies are the largest gravitational entities of the Universe and their formation occurs at early epochs ($z \gtrsim 1$). Observations of forming clusters at high redshifts require long exposures and involve crucial technical difficulties. Nearby systems can still provide critical information about the structural formation; however, the evolutionary effects should be considered cautiously.

The dynamical consequence of a cluster merger is the transfer of energy ($\gtrsim 10^{64}$ erg s^{-1}) and angular momentum of the merging subclusters to the system. The collisional nature of the hot plasma and the non-collisional nature of the galaxies result in different reaction time-scales during a merger (e.g. White & Fabian 1995; Roettiger, Loken & Burns 1997). In such merging conditions, the extended inter-cluster medium (ICM) is strongly affected, while individual galaxies can pass through. The brightest cluster galaxy (BCG) is defined as the brightest galaxy in a cluster. BCGs are generally elliptical and are expected to be at the bottom of the potential well of the parent cluster (e.g. Quintana & Lawrie 1982; Adami et al. 1998; Adami & Ulmer 2000). The merger of BCG-hosting clusters creates velocity offsets and dislocates the BCG from the dynamical centre. Several observations have identified displaced BCGs from the cluster centre (e.g. Smith et al. 2005; Shan et al. 2010) and a number of BCGs with a significant velocity gradient from the cluster mean (see e.g. Beers et al. 1991). A velocity comparison can determine the system's deviation from a relaxed configuration. Density maps, which are produced with position and velocity information for cluster member galaxies, also reveal the footprints of substructures (e.g. Quintana et al. 1996; Barrena et al. 2009; Shakouri, Johnston-Hollitt & Dehghan 2016).

With the recent improvements of high angular resolution cameras, X-ray observations have played a key role in investigating merging clusters. The fate of the merger energy and the complexity of the collisional ICM have been considerably settled. Apparently, the kinetic energy of the merging structures is converted into thermal energy of the plasma, which has been observed in many clusters (e.g. Markevitch & Vikhlinin 2007; Bourdin & Mazzotta 2008).

In this paper, we present structural analysis results for Abell 3653 (A3653). The cluster's BCG has one of the most extreme radial velocities (Pimbblet, Roseboom & Doyle 2006), which strongly suggests recent or ongoing merger activity. The original optical data were studied for signs of a substructure by Pimbblet et al. (2006), but they did not report any significant grouping. A3653

★ E-mail: hudaverd@yildiz.edu.tr

was also studied in the *MCMX* meta-catalogue based on the *ROSAT* All Sky Survey (Piffaretti et al. 2011). *MCMX* provides a redshift of 0.1069, a standardized 0.1–2.4 keV band luminosity of $L_{500} = 1.57 \times 10^{44}$ erg s^{-1}, a total mass of $M_{500} = 2.5 \times 10^{14}$ M$_{\odot}$ and a radius of $R_{500} = 925.8$ kpc. To understand the dynamical structure of A3653, we investigate its X-ray morphology and temperature distribution with archival *XMM–Newton* and *Chandra* observations. A raw X-ray image shows a clear bimodal structure with X-ray centroids: A3653E (J2000, RA 19^{h}53^{m}01^{s}.9, Dec. −52°02′13″) and A3653W (J2000, RA 19^{h}52^{m}17^{s}.3, Dec. −51°59′50″) (see Fig. 2).

In this study, we aim to describe the X-ray morphology and temperature structure of Abell 3653. Moreover, we focus on explaining the physical mechanism of the dynamical merge activities. We compare our X-ray results with the optical results studied by Pimbblet et al. (2006). The optical study indicates that A3653 has 111 galaxies in the cluster field. A3653 is located at RA 19^{h}53^{m}00^{s}.9 and Dec. −52°01′51″ and it has a redshift (z) of 0.1089 (Struble & Rood 1999). In addition, A3653 is a rich centrally condensed cluster (Gregorini et al. 1994).

This paper is organized as follows. In Section 2, we describe the data used in our analysis. In Section 3, the analysis of the X-ray and optical observations is described and the temperature distribution is studied in detail. In Section 4, we discuss the cluster dynamics and possible subclusters. We summarize our results in Section 5. We adopt cosmological parameters $H_0 = 70$ km s^{-1} Mpc^{-1}, $\Omega_M = 0.27$ and $\Omega_\Lambda = 0.73$ in a flat universe. For this cosmology, an angular size of 1 arcmin corresponds to a physical scale of 119.22 kpc at the redshift of A3653 ($z = 0.1089$). Unless otherwise stated, the reported errors correspond to 90 per cent confidence intervals.

2 OBSERVATIONS AND DATA REDUCTION

2.1 Optical spectroscopic data

We obtained galaxy spectroscopic redshifts using the Anglo-Australian Telescope (AAT). In the literature, there are several studies of velocity measurements for a variety of samples. We selected galaxies within a 3.0 Mpc radius of the A3653 centroid with a spectroscopic redshift falling in the interval $0.099 < z_{spec} < 0.115$, which fairly captures the range of galaxies associated with A3653. Our selection includes 87 members: 83 galaxies from the 2dF (Pimbblet et al. 2006) and four galaxies from the 6dF Galaxy Survey final red shift release (Jones et al. 2009). The member galaxies are listed in the appendix.

A projected galaxy density map of the member galaxies is shown in Fig. 1 (left-hand panel). Galaxies identified as cluster members from spectroscopy are marked with dots. The two plus signs are the locations of the BCGs. Two circles, superimposed as a visual aid, show the extended X-ray count extraction regions used for the spectral analysis. The galaxy density distribution shows an elongated structure with an east–west axis with a little tilt.

Based on 87 redshifts we plot a redshift histogram of A3653 (see Fig. 1, right-hand panel). The vertical dotted line shows the mean cluster red shift of $z = 0.1089$. The cluster's BCG has one of the most extreme radial velocities: $\sigma_{cz} = 683 \pm 96$ km s^{-1} away from the mean cluster velocity (Pimbblet et al. 2006), which locates it considerably further at $z = 0.1099$. Although a Gaussianity is visible around the cluster mean $z = 0.1089$, deviations from a single Gaussian can be attributed to the subclusters around two BCGs. BCG1 at $z = 0.1099$ can be associated with the main cluster, and there is a foreground western clump concentrated around the galaxy 2MASX J19521735-5159465 at $z = 0.1075$ (Jones et al. 2009). This galaxy is catalogued with $(r_F, b_J) = (15.20, 16.11)$ magnitudes in the NASA Extragalactic Database. Considering its location at the X-ray centroid of A3653W and being two magnitudes brighter than neighbouring members, 2MASX J19521735-5159465 is called BCG2 hereafter. BCG2 was unexpectedly not included in the 2dF Galaxy Survey study of Pimbblet et al. (2006). This is possibly why the cD galaxy of A3653 and its peculiar velocity could not be explained with any significant grouping. The redshifts of the two BCGs are indicated in the histogram (Fig. 1, right-hand panel). Since we are interested in the potential subgroups associated with merger scenarios, we also identify the galaxies clustering around BCG2 with $V_r = 32\,221 \pm 350$ km s^{-1} ($0.10625 < z < 0.10875$), as

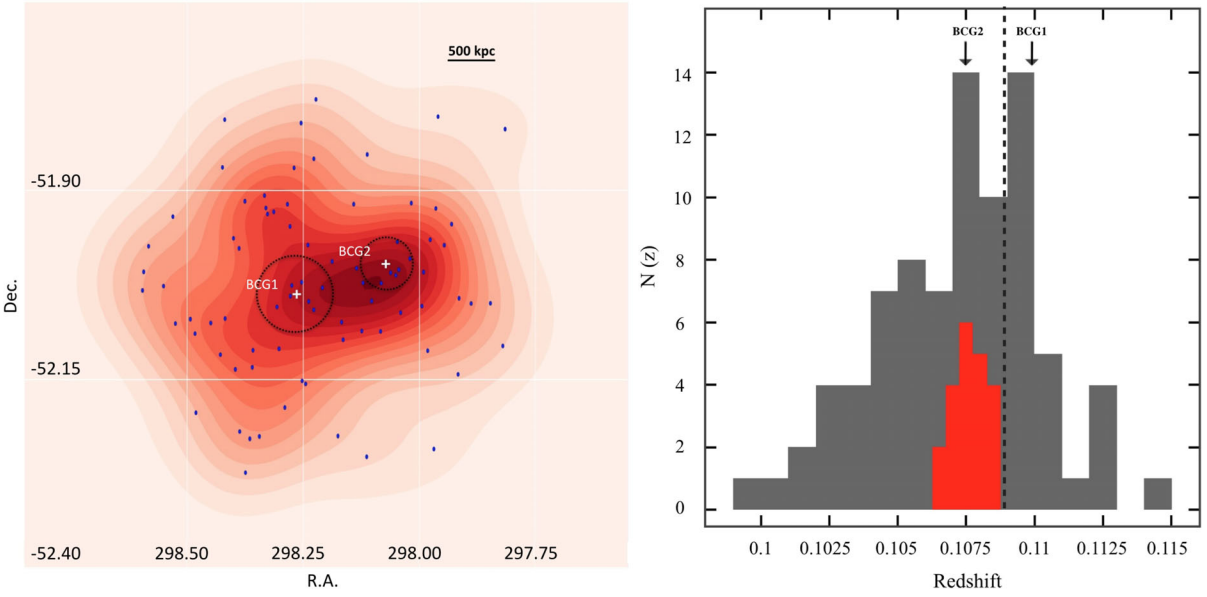

Figure 1. Left: Galaxy density map of A3653 within a 1.5 Mpc radius field. The white crosses indicate the BCG positions. Right: redshift histogram for 84 member galaxies of A3653. The vertical dotted line gives the mean cluster value, and the two arrows indicate the redshifts of the BCGs. The red histogram shows the member galaxies around BCG2 ($0.10625 < z < 0.10875$).

Table 1. Log of X-ray observations.

Observation ID	Satellite	Date observed	Effective exposure time (ks)
10460	*Chandra*	2009 July 5	ACIS 43.6 (98.6 per cent)
0691820101	*XMM–Newton*	2013 March 18	MOS1 48.6 (75.2 per cent)
			MOS2 48.8 (75.5 per cent)
			PN 47.5 (78.3 per cent)

displayed in Fig. 1 (right, red). Their spatial properties are discussed with the X-ray analysis results in later sections.

2.2 X-ray observations

We used *XMM–Newton* and *Chandra* archival data for our analysis (see Table 1). The *XMM–Newton* observation was made on 2013 March 19 for an exposure time of 64 ks with observation ID 0691820101. The MOS and PN detectors were in full frame mode and extended full frame, respectively, with the thin filter. Observation data were obtained from the XMM–Newton Science Archive. We performed the data processing and background modelling with the XMM Extended Source Analysis Software (XMM-ESAS) (Snowden et al. 2008) and *XMM–Newton* Scientific Analysis System (XMMSAS) v14.0. The event files for MOSs and PN were created using EMCHAIN and EPCHAIN, respectively. We filtered bad pixels, bad columns and cosmic rays using EVSELECT. The total filtered MOS1, MOS2 and PN exposure times are 48.6, 48.8 and 47.5 ks, respectively.

The *Chandra* observation of A3653 was carried out on 2009 July 5 (observation ID 10460) for a total exposure of 44.2 ks with CCDs 3, 5, 6, 7 and 8 of the Advanced CCD Imaging Spectrometer (ACIS), telemetered in the VFAINT mode. We obtained observation data from the Chandra Data Archive. Most of the X-ray emissions of A3653 are covered by the AICS-S3 chip. Therefore, this study focuses on the S3 chip. The data were reprocessed from level 1 event files using CIAO 4.8 and CALDB 4.7.0. The total altered ACIS exposure time is 43.6 ks.

3 ANALYSIS

We generated broad-band images from *XMM–Newton* in the 0.3–10 keV and *Chandra* in the 0.5–7 keV ranges, respectively. Fig. 2 shows adaptively smoothed images. The left-hand panel is the *XMM–Newton* MOSs/PN mosaic image, which is without exposure or background correction. The exposure-corrected *Chandra* image of the extended diffuse emission for A3653 was created using FLUXIMAGE (Fig. 2, right panel). The *XMM–Newton* observation covers almost the entire cluster emission, while the narrow field-of-view (FOV) of *Chandra* ACIS-S3 collects photons only from the main cluster. The tilted square in the *XMM–Newton* image shows the ACIS-S3 FOV, and the two circles are the X-ray emission regions selected for the global spectral analysis. The subclusters do not have bright central cores or regular morphologies, as is typical of non-cool core clusters.

The locations of the point sources in the FOV are detected using EDETECT_CHAIN in the 0.2–12 keV energy band for *XMM–Newton*. For *Chandra* data, we used CIAO's WAVDETECT in the 0.5–8 keV energy band. We excluded all point sources at 4σ confidence level by masking the event files and thereby decreasing the contribution of point sources to the extended ICM emission.

Fig. 3 shows the contours from the combined MOS images in the 0.3–10 keV energy band, overlaid on the Digitized Sky Survey (DSS) optical image for A3653. Since the PN image is disrupted by chip gaps at the central regions (see Fig. 2), we rejected PN data for imaging and the related analysis. The X-ray image was adaptively smoothed and corrected for the background, exposure time and vignetting. Two regions used for the spectral extraction for the subcluster extended emission are indicated with dashed circles. The positions of the subcluster X-ray peaks (A3653E and A3653W) are indicated by plus signs. BCG1 and BCG2 are indicated by arrows to underline their evident relations with A3653E and A3653W, respectively. However, the X-ray peaks do not exactly match the BCGs and there is a clear shift of ∼35 kpc for both. This type of positional disturbance can be associated with an ongoing merger activity, which may dislocate the BCGs from the dynamical centre. The cluster member galaxies from spectroscopy are marked with circles.

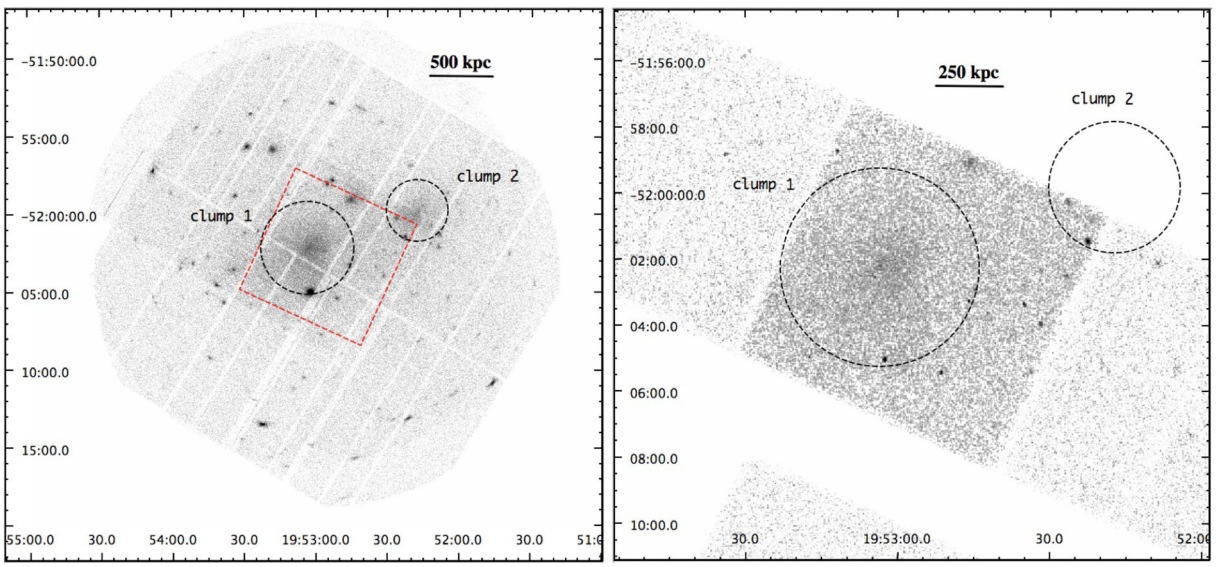

Figure 2. Left: Mosaic *XMM–Newton* MOSs/PN image in the 0.3–10 keV energy range. Right: Background and exposure-corrected *Chandra* ACIS-S3 image in the 0.5–7 keV energy range. The spectrum extraction regions for the subclusters are denoted with the circles. The tilted square region on the *XMM*–Newton image corresponds to the *Chandra* FOV. The images are adaptively smoothed to highlight the structures with extended plasma emission.

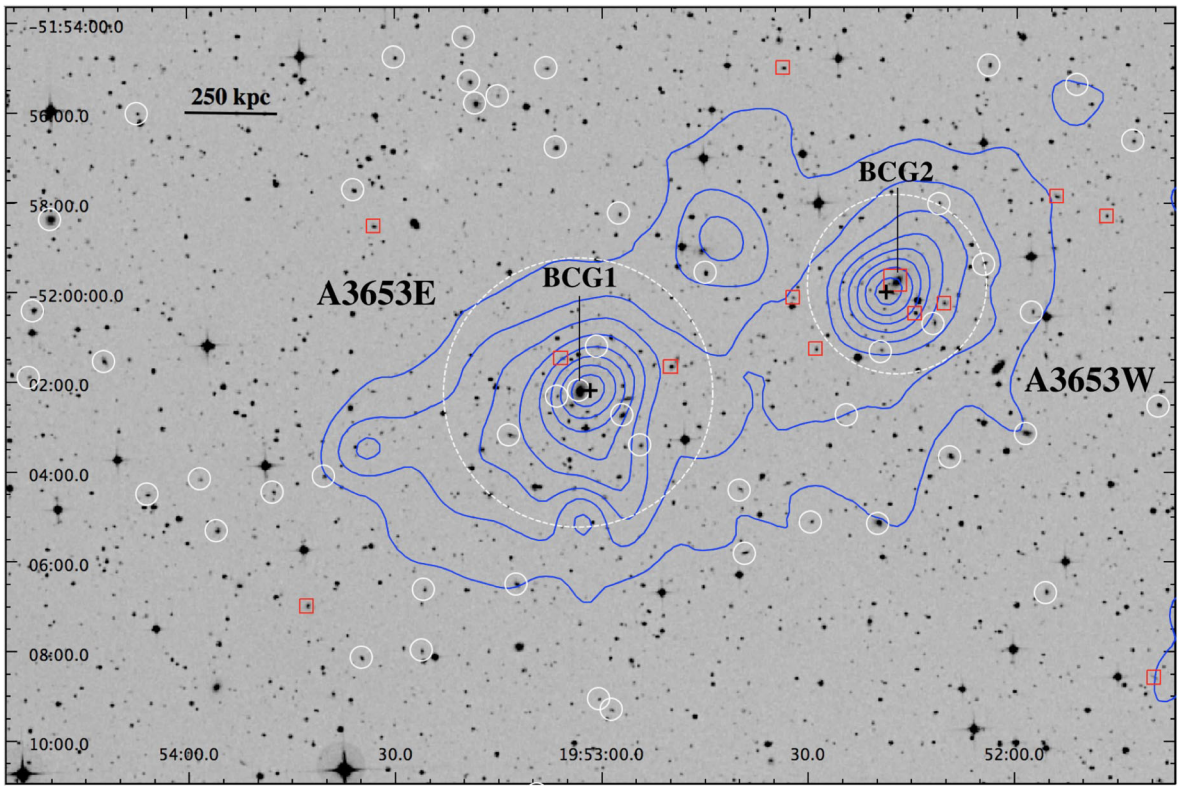

Figure 3. Contours of the X-ray diffuse emission at 0.3–10 keV from MOS logarithmically spaced by a factor of 0.7 and overlaid on the DSS optical image. The subclusters are indicated with dashed circles. The positions of the subcluster X-ray peaks are indicated by plus signs, and the associated BCGs are indicated by arrows. The galaxies identified as cluster members are marked with white circles. The red boxes indicate the galaxies with $V_r = 32\,221 \pm 350\,\mathrm{km\,s^{-1}}$ around BCG2.

The red boxes are the members of the sub-sample, which has redshifts clustering at the red shift of A3653W ($z = 0.1075 \pm 0.0012$). At this redshift range, there are 21 members but these are spatially dispersed, which means it is not straightforward to determine an optical subcluster.

3.1 Spectral analysis

We examined the spectra of each subcluster to determine the global properties of the ICM. The spectrum of A3653E is extracted and studied for *XMM–Newton* and *Chandra*, since it is clearly viewed from both cameras. The western subcluster A3653W is analysed only by *XMM–Newton* due to a lack of *Chandra* observations in that region. *XMM–Newton* spectra and response files were generated using EVSELECT V3.62, RMFGEN V2.2.1 and ARFGEN V1.90.4. An annular region 11–12 arcmin away from the cluster centroid is used to extract the local background. To model the background, we used the CALDB blank sky event files for *Chandra*. The spectral files are generated using SPECEXTRACT. The spectra from the observations were fitted using the XSPEC software package, version 12.9.0 (Arnaud 1996). Temperature and abundance were allowed to be free parameters. We adopt the solar abundance table from Anders & Grevesse (1989). Varying the galactic absorption column density did not significantly influence the primary parameters or improve the spectral fits. Therefore, in all cases, the value is fixed at that for the position on the sky of A3653 from the Leiden/Argentine/Bonn (LAB) Survey (Kalberla et al. 2005), $N_H = 4.14 \times 10^{20}\,\mathrm{cm^{-2}}$.

For *XMM–Newton* data, energies outside the range 0.3–10 keV were ignored. The EPIC-MOS and PN spectra were fitted simultaneously, after checking the consistency. The bright instrumental lines due to the quiescent particle background (QDP) – Al-K α (1.49 keV) and Si-K α (1.74 keV) for MOS, and Al-K α and Cu-K α (8.05, 8.91 keV) for PN – are carefully ignored from the spectral data. The *Chandra* fitting was performed in the 0.5–7 keV energy range. The blank sky event files were normalized in the 10–12 keV band to the count rate of the observations to account for the QDP. We used an absorbed single-temperature collisional equilibrium plasma (APEC) model. For subcluster A3653E, the model gives a temperature of $kT = 4.67 \pm 0.20$ keV and an abundance of $Z = 0.14 \pm 0.05\,Z_\odot$ for *XMM–Newton*. For the same region, the best-fitting parameters for the *Chandra* data are highly consistent within the error range; the temperature is $kT = 4.67 \pm 0.46$ keV and the abundance is $Z = 0.20^{+0.14}_{-0.13}\,Z_\odot$. Since we lacked *Chandra* observations, the spectral modelling is performed only for *XMM–Newton* data for the western subcluster, A3653W. The best-fitting parameters for the spectral modelling within 2.5 arcmin radius circle are $kT = 3.66^{+0.29}_{-0.28}$ keV for temperature $Z = 0.27^{+0.09}_{-0.08}\,Z_\odot$ for the abundance. The results from the spectral fitting are summarized in Table 2.

3.2 Temperature map

Temperature maps are very powerful tools, which provide useful information about temperature discontinuities due to the ongoing merger. To search for evidence, we generated a temperature map for A3653 with the hardness ratio approximation. The images were carefully extracted in the soft and hard energy bands by avoiding QDP instrumental lines, galactic absorption of soft bands

Table 2. The best-fitting parameters for the spectral modelling of A3653 subclusters.

Region	kT (keV)	Abundance ($Z_\odot$)	χ^2/dof
A3653E[a]	4.67 ± 0.20	0.15 ± 0.05	$2162/1760 = 1.23$
A3653E[b]	4.67 ± 0.46	$0.24^{+0.14}_{-0.13}$	$289/251 = 1.15$
A3653W[a]	$3.66^{+0.29}_{-0.28}$	$0.27^{+0.09}_{-0.08}$	$1241/1223 = 1.01$

Notes. [a]*XMM–Newton* data; [b]*Chandra* data.

(<0.7 keV) and point source emissions of hard bands (>8 keV). Point sources were excluded from the event files used for the analysis, and the holes were filled using the surface brightness of the surrounding pixels with the CIAO tool DMFILT. The total energy photon counts divided into equal two energy bands to define the soft and the hard energy images. The hardness ratio maps are produced by the images for energy bands 0.8–1.6 keV and 1.8–8 keV from *XMM–Newton* MOSs, and 0.7–1.6 keV and 1.6–7 keV for *Chandra* ACIS-S3 counts, respectively. The hard images are divided by the corresponding soft images to obtain a hardness ratio map. The pixel ratios of the map are converted to temperature values by multiplying by theoretical conversion factors. The factors are determined using an absorbed single thermal collisional plasma model (WABS × APEC), with a column density fixed to the Galactic value of $N_{\rm H} = 4.14 \times 10^{20}$ cm^{-2}, and a red shift of $z = 0.1089$. A similar technique for producing a temperature map from a hardness ratio is outlined in Ferrari et al. (2006).

Fig. 4 shows the temperature map obtained through the hardness ratio technique for *XMM–Newton* (left) and *Chandra* (right). The vertical colour-coding for the temperature maps has the same scale for both, which ranges from black (∼4 keV) to yellow (∼6 keV). The *Chandra* and *XMM–Newton* temperature structure and the variation display similar properties within the common frame, which is shown with a square in the left panel. Based on the temperature map, A3653 is characterized by two cold regions (∼3.5 to 4.5 keV) associated with A3653E and A3653W, and a hot region (∼6 keV) in between.

The confidence of the temperature map is spectroscopically confirmed for five control regions (labelled A, B, C, D and E), as shown in Fig. 4. The spectroscopic temperature values ($T_{\rm spec}$) are estimated from the *XMM–Newton* MOSs/PN simultaneous fit with $N_{\rm H}$ fixed to the galactic value, and provide a reduced $\chi^2 \simeq 1$. Table 3 compares these best-fitting temperature values ($T_{\rm spec}$) with the values obtained directly from the temperature maps ($T_{\rm map}$). The values are in good agreement within the error range. Fig. 5 shows a plot of $T_{\rm spec}$ versus $T_{\rm map}$ and visually confirms the consistency. The ratios vary neatly around 1 (inclined line), for which $T_{\rm spec}$ and $T_{\rm map}$ are equal.

Table 3. Comparison of the temperature map ($T_{\rm map}$) values with spectroscopically derived temperatures ($T_{\rm spec}$).

Region	$T_{\rm map}$ (keV)	$T_{\rm spec}$ (keV)	χ^2/dof
A	4.21 ± 0.49	$4.30^{+0.34}_{-0.28}$	$1166/1122 = 1.03$
B	3.66 ± 0.63	$3.78^{+0.36}_{-0.35}$	$717/693 = 1.03$
C	6.08 ± 0.99	$6.16^{+1.40}_{-1.20}$	$373/364 = 1.02$
D	5.98 ± 0.97	$6.06^{+1.20}_{-1.10}$	$575/485 = 1.18$
E	3.65 ± 0.57	$3.38^{+0.49}_{-0.53}$	$240/241 = 1.00$

The temperature map study and related spectral analysis results verify that A3653E (4.67 keV) and A3653W (3.66 keV) have relatively cool cores. There is a significantly hot (6.16 keV) distinct region between the subclusters. If we assume that the subclusters are gravitationally bound and moving towards each other, the hot region seems like it has been shock-heated by a possible merger event.

4 MASS ANALYSIS

The mass of isothermal clusters is estimated to scale with the X-ray emission-weighted temperature by $M \propto T_x^{3/2}$, as predicted by simulations (e.g. Eke, Cole & Frenk 1996) and observations (e.g. Markevitch 1998). A similar assumption gives us a mass ratio of 1.4:1.

The masses were also quantitatively estimated using the M versus T relation derived without groups by Finoguenov, Reiprich & Böhringer (2001):

$$M_{500} = \left(3.57^{+0.41}_{-0.35}\right) \times 10^{13} \times kT_{\rm ew}^{1.58^{+0.06}_{-0.07}}. \quad (1)$$

A3653E has a best-fitting global temperature of 4.67 ± 0.20 keV and an abundance of $0.15 \pm 0.05\,Z_\odot$. The scaling relation

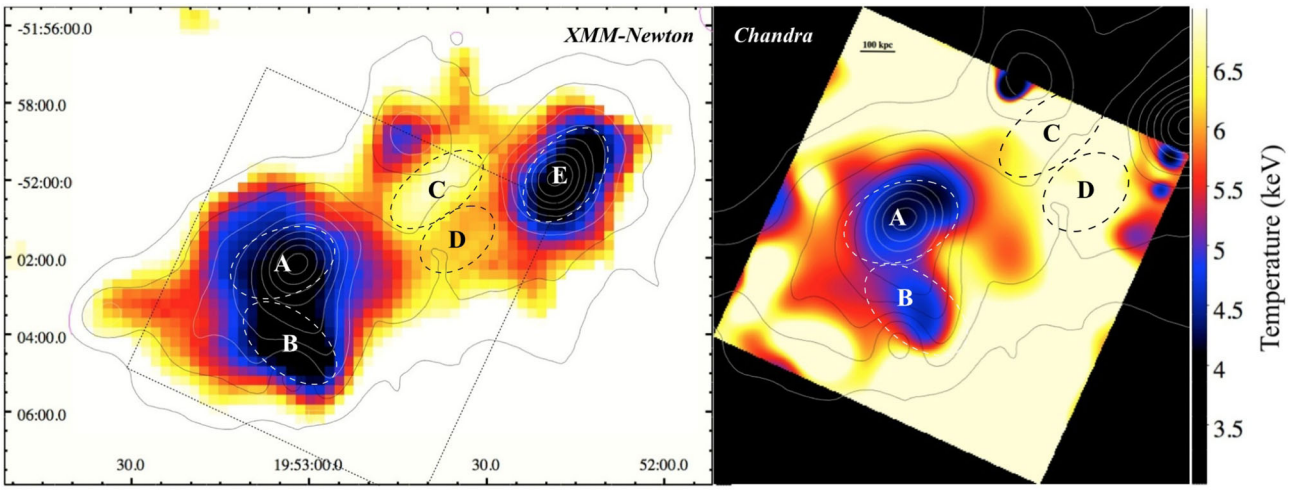

Figure 4. Temperature map obtained with the hardness ratio approximation method for *XMM–Newton* (left) and *Chandra* (right) (see Section 3.2 for details). The colour-coding ranges are from black (∼4 keV) to yellow (>6 keV). X-ray contours (as in Fig. 3) are superimposed as a visual aid. The tilted square shows the *Chandra* FOV. The regions used for the spectroscopic analysis are in ellipses.

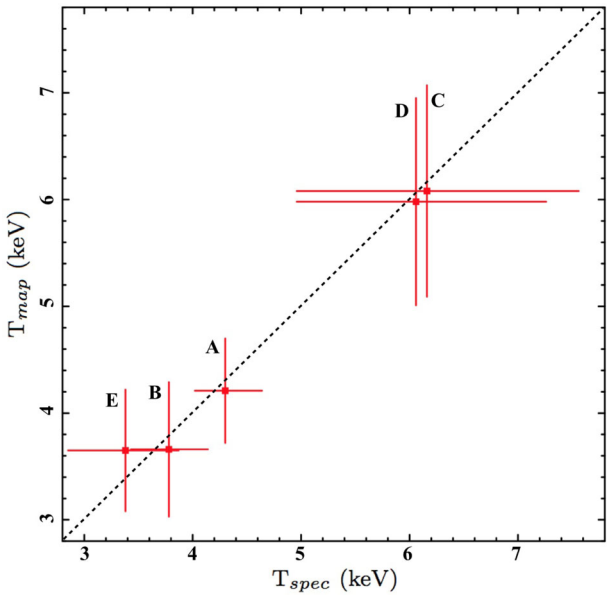

Figure 5. Plot of $T_{\rm spec}$ versus $T_{\rm map}$ for five peculiar regions. The ratios vary around 1 (inclined line), which confirms the consistency and the agreement of the values.

Table 4. Properties of the A3653 system.

Parameter	A3653E	A3653W
z	0.1099 ± 0.0002^a	0.1075 ± 0.0002^b
$V_{\rm r}$ (km s^{-1})	$32\,947 \pm 66^a$	$32\,221 \pm 45^b$
M ($M_\odot$)	4.06×10^{14}	2.77×10^{14}

[a] Pimbblet et al. (2006); [b]Jones et al. (2009).

estimates a total mass of $4.06 \times 10^{14}\,M_\odot$ for the A3653E subcluster. The best-fitting temperature of A3653W is $3.66^{+0.29}_{-0.28}$ keV, with an abundance of $0.27^{+0.09}_{-0.08}\,Z_\odot$. The scaling relation predicts a total mass of $2.77 \times 10^{14}\,M_\odot$ for A3653W. These numeric mass estimations also give a mass fraction of ∼1.4, consistently. Table 4 lists the redshifts the relative velocity of the BCGs and the total masses of the A3653 subclusters.

5 A DYNAMICAL MODEL FOR A3653E AND A3653W

We apply the Newtonian gravitational binding criterion that a two-body system is bound if the potential energy of the system is equal to or greater than the kinetic energy. The two-body dynamical model was described in detail by Beers, Geller & Huchra (1982) and Gregory & Thomson (1984). The model has also been successfully applied to several bimodal systems in the literature, e.g. A1367 (Cortese et al. 2004), A168 (Hwang & Lee 2009), A2319 (Yan et al. 2014), A3716 (Andrade-Santos et al. 2015), A3407 and A3408 (Nascimento et al. 2016), and A1750 (Hwang & Lee 2009; Bulbul et al. 2016). This model allows us to evaluate the dynamical state of A3653E and A3653W and to estimate the probability that (i) the system is infalling, (ii) the system is gravitationally bound but still expanding, or (iii) the subclusters are unbound but are projectionally close together in the sky by chance.

The limits of the bound solutions for a system can be determined using the Newtonian criterion for gravitational binding (Beers et al. 1982):

$$V_{\rm r}^2 R_p \leq 2GM \sin^2\alpha \cos\alpha. \tag{2}$$

The radial velocity difference, $V_{\rm r}$, and the projected separation, R_p, are related to the real velocity and separation of the system parameters by

$$V_{\rm r} = V \sin\alpha, \quad R_p = R\cos\alpha. \tag{3}$$

The angle α is the projection angle between the plane of the sky and the line connecting the subsystems (i.e. $\alpha = 0$ if the subclusters are at the same distance). V and R are the true (3D) velocity and positional separation between the two subclusters. For gravitationally bound systems, the parametric solutions to the equation of motion (Beers et al. 1982) are

$$t = \left(\frac{R_m^3}{8GM}\right)^{1/2} (\chi - \sin\chi), \tag{4}$$

$$R = \frac{R_m}{2}(1 - \cos\chi) \tag{5}$$

and

$$V = \left(\frac{2GM}{R_m}\right)^{1/2} \frac{\sin\chi}{(1-\cos\chi)}, \tag{6}$$

where R is the separation at time t, R_m is the separation at the maximum expansion, M is the combined mass of the system and χ is the developmental angle.

Similarly, the parametric solutions for the unbound case are also described by Beers et al. (1982). For gravitationally unbound systems, the parametric equations are

$$t = \frac{GM}{V_\infty^3}(\sinh\chi - \chi), \tag{7}$$

$$R = \frac{GM}{V_\infty^2}(\cosh\chi - 1) \tag{8}$$

and

$$V = V_\infty \frac{\sinh\chi}{(\cosh\chi - 1)}, \tag{9}$$

where V_∞ is the asymptotic expansion velocity. Using the parameters previously found for the A3653 subclusters – a radial velocity difference of $V_{\rm r} = 726 \pm 80\,{\rm km\,s^{-1}}$, a projected distance ($R_p$) on the plane of the sky between the X-ray centres of the subclusters of 0.89 Mpc, a total mass of $M = 6.83 \times 10^{14}$ (see Table 4), and setting $t = 12.1$ Gyr (3.8×10^{17} s), which is the age of the universe at the A3653 red shift – we can constrain the equations.

Subsequently, the radial velocity difference ($V_{\rm r}$) as a function of the projection angle (α) between the subclusters can be solved by equation (6) of Gregory & Thomson (1984) for the bound and unbound states:

$$\tan\alpha = \frac{tV_{\rm r}}{R_p}\frac{(\cos\chi - 1)^2}{\sin\chi(\chi - \sin\chi)} \tag{10}$$

and

$$\tan\alpha = \frac{tV_{\rm r}}{R_p}\frac{(\cosh\chi - 1)^2}{\sinh\chi(\sinh\chi - \chi)}, \tag{11}$$

respectively.

The solution for the A3653 system is shown in Fig. 6. The projected angle (α) as a function of the radial velocity difference ($V_{\rm r}$) is

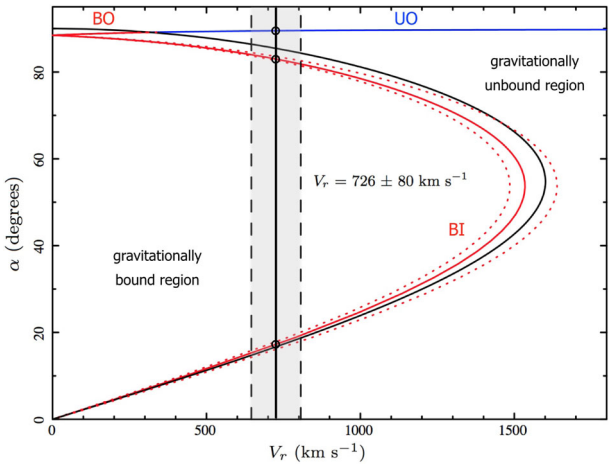

Figure 6. Projection angle (α) as a function of the relative radial velocity difference (V_r) of the subclusters A3653E and A3653W. BI, BO and UO stand for bound-incoming, bound-outgoing and unbound-outgoing solutions. The red and blue lines correspond to bound and unbound solutions, respectively. The black curve separates the bound and unbound regions according to the Newtonian criterion. The vertical lines represent the relative radial velocity, $V_r = 726 \pm 80\,\mathrm{km\,s^{-1}}$, between the two clusters in the rest frame of A3653. The black circles are the three acceptable solutions.

plotted for bound (red line) and unbound (blue line) solutions. The black curve separates the bound and unbound regions according to the Newtonian criterion.

Since the relative radial velocity of our system is observed to be $V_r = 726 \pm 80\,\mathrm{km\,s^{-1}}$, we obtain two bound solutions and one unbound solution. All three solutions (black circles in Fig. 6) are defined by the intersections of curved lines with the solid vertical line corresponding to the relative velocity difference ($V_r = 726 \pm 80\,\mathrm{km\,s^{-1}}$) between the two clusters in the rest frame of A3653. The uncertainties in the measured velocity lead to a range of solutions from α_{inf} to α_{sup} for the projection angles. We compute the relative probabilities for the solutions with the formula (Girardi et al. 2005):

$$p_i = \int_{\alpha_{\mathrm{inf},i}}^{\alpha_{\mathrm{sup},i}} \cos\alpha \, \mathrm{d}\alpha, \qquad (12)$$

where each solution is represented by index i. The probabilities are normalized by $P_i = p_i/(\sum_i p_i)$.

Solving the parametric equations, we get two gravitationally bound incoming solutions and one unbound outgoing solution. For the bound solutions, the subclusters are either approaching each other at 732 km s^{-1} (6.5 per cent probability) or at 2400 km s^{-1} (93.5 per cent probability). The first solution suggests that the subcluster cores will cross each other after a long time (9.7 Gyr) given a separation of 7.24 Mpc with a mean colliding velocity of 732 km s^{-1}. This bound scenario apparently does not predict a strong interaction between A3653E and A3653W, thus the solution has a low probability (6.5 per cent). The latter and more likely scenario corresponds to a collision in about 380 Myr, considering their separation of 0.93 Mpc with a supersonic colliding velocity of 2400 km s^{-1}. The temperature map (Fig. 5) also confirms there is a hot region and the spectral fit gives $kT = 6.16^{+1.40}_{-1.20}$ keV, providing evidence of shock-heated gas between the subclusters. The large-angle ($\alpha = 89.49°$) unbound solution (0.05 per cent probability) corresponds to a separation of 71.3 Mpc. The parameters of these solutions are presented in Tables 5 and 6. Given its negligibly low probability, the unbound solution can be disregarded, while the bound solution close to the plane of the sky ($\alpha = 17.61°$) is highly favoured (93.5 per cent probability).

Table 5. Best-fitting parameters for the bound incoming solutions of the dynamical model. The columns list the best-fitting values for χ and α for the bound solutions, and the corresponding values for R, R_m, V and the related probabilities P.

χ (rad)	α (degrees)	R (Mpc)	R_m (Mpc)	V (km s^{-1})	P (per cent)
5.05	82.94	7.24	21.50	731.5	6.5
5.86	17.61	0.93	20.88	2399.7	93.5

Table 6. Best-fitting parameters for the unbound outgoing solutions of the dynamical model. The columns list the best-fitting values for χ and α for the bound solutions, and the corresponding values for R, V, V_∞ and the related probabilities P.

χ (rad)	α (degrees)	R (Mpc)	V (km s^{-1})	V_∞ (km s^{-1})	P (per cent)
3.16	89.49	71.30	726.03	666.88	0.02

The dynamical model analysis result for A3653 is fairly conclusive in stating that the subclusters are very likely gravitationally bound, and the cores will cross each other in 380 Myr. Normally, approaching systems produce a strong ram pressure and the X-ray plasma is displaced (Vijayaraghavan & Ricker 2013). In our case, the X-ray peaks are found to be in the opposite direction. This suggests that this is not the first encounter of the subclusters; therefore, there was a previous core passage. The probabilities for the bound solutions should be treated cautiously, since the dynamical two-body model assumes a clear radial infall (e.g. a head-on merger) and does not include the angular momentum information of the subclusters, which is very unlikely to be zero. If the merger of the subclusters occurs with angular momentum, as in off-axis mergers, the consequences will be more complicated, as shown in the simulations (Takizawa 2000; Vijayaraghavan & Ricker 2013).

6 SUMMARY

We present the analysis results of a merging binary cluster A3653 using AAT Optical Galaxy Survey data, *XMM–Newton* and *Chandra* X-ray observations. Spectroscopic redshift analysis, X-ray brightness and temperature maps and two-body dynamical model analysis clearly indicate that A3653 is not a single structure but composed of two subclusters. A possible interpretation of our findings is illustrated in Fig. 7. Our main results are:

(i) Based on the optical spectroscopic redshifts of 87 member galaxies in AAT Galaxy Survey data, A3653 has a mean cluster red shift of $z = 0.1089$. We detect two dominant groups of member galaxies. BCG1 at $z = 0.1099$ can be associated with the main cluster and BCG2 is a little foreground western subgroup concentrated at $z = 0.1075$ (Fig. 1).

(ii) The X-ray brightness map also clearly indicates the binary structure of A3653 with two distinct clumps (see Fig. 2). The X-ray peaks match with the BCGs with a small disturbance (∼35 kpc), which is probably caused by the ram pressure of ongoing dynamical activity (see Fig. 3). The displacement of the peaks is aligned with the elongation of the subcluster locations,

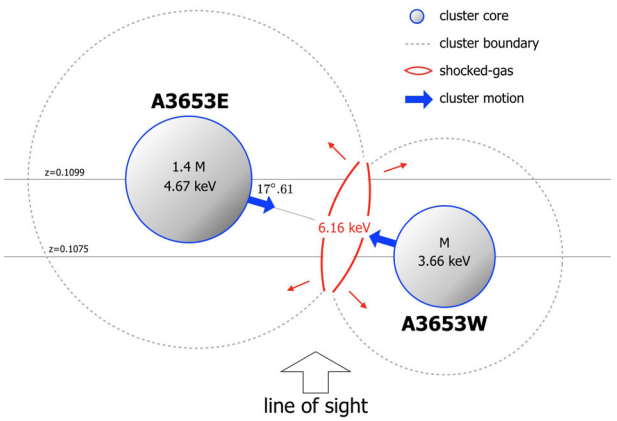

Figure 7. Tentative illustration of subclusters A3653E and A3653W gravitationally falling into each other (blue arrows). The merger is happening very close to the plane of the sky (horizontal lines). The cluster boundaries (dotted circles) have started to collide and a shocked region has developed (in red). The line of sight is depicted with a big arrow at the bottom.

which suggest that the peak shifts are associated with the merger activity. However, the position of the peaks implies that there was a previous core passage between the subclusters.

(iii) The average temperatures of A3653E and A3653W are 4.67 and 3.66 keV, respectively. Based on the temperature map, we detect a possible shock-heated gas with a significantly elevated temperature of $kT = 6.16$ keV between the two subclusters (see Fig. 4). The hot gas results from shock-heating by the merging subclusters.

(iv) Mass calculations for isothermal clusters result in $M_{\rm A3653E} = 4.06 \times 10^{14}\,{\rm M}_{\odot}$ and $M_{\rm A3653W} = 2.77 \times 10^{14}\,{\rm M}_{\odot}$. A3653 is composed of two merging subclusters with ∼1.4 mass fraction.

(v) The two-body dynamical model suggests three solutions: two collapsing and one unbound expanding (see Fig. 6). Based on the analysis, the unbound solution has a negligibly low (0.02 per cent) probability. The subclusters are gravitationally bound and infalling. The merger is happening close to the plane of the sky ($\alpha = 17.61^{\circ}$), and the cores will cross each other in 380 Myr.

ACKNOWLEDGEMENTS

We would like to acknowledge financial support from the Scientific and Technological Research Council of Turkey (TÜBİTAK), project number 113F117. The work is also supported by YTU Scientific Research and Project Office funding under contracts 2013-01-01-YL01 and 2013-01-01-KAP04. The authors would like to thank S. Alis for a useful discussion and suggestions.

REFERENCES

Adami C., Ulmer M. P., 2000, A&A, 361, 13
Adami C., Mazure A., Katgert P., Biviano A., 1998, A&A, 336, 63
Anders E., Grevesse N., 1989, GeCoA, 53, 197
Andrade-Santos F. et al., 2015, ApJ, 803, 108
Arnaud K. A., 1996, ASPC, 101, 17
Barrena R., Girardi M., Boschin W., Dasí M., 2009, A&A, 503, 357
Beers T. C., Geller M. J., Huchra J. P., 1982, ApJ, 257, 23
Beers T. C., Gebhardt K., Forman W., Huchra J. P., Jones C., 1991, AJ, 102, 1581
Bourdin H., Mazzotta P., 2008, A&A, 479, 307
Bulbul E. et al., 2016, ApJ, 818, 131
Cortese L., Gavazzi G., Boselli A., Iglesias-Paramo J., Carrasco L., 2004, A&A, 425, 429
Eke V. R., Cole S., Frenk C. S., 1996, MNRAS, 282, 263
Ferrari C., Arnaud M., Ettori S., Maurogordato S., Rho J., 2006, A&A, 446, 417
Finoguenov A., Reiprich T. H., Böhringer H., 2001, A&A, 368, 749
Girardi M., Demarco R., Rosati P., Borgani S., 2005, A&A, 442, 29
Gregorini L., de Ruiter H. R., Parma P., Sadler E. M., Vettolani G., Ekers R. D., 1994, A&A, 106, 1
Gregory S. A., Thompson L., 1984, ApJ, 286, 422
Hwang H. S., Lee M. G., 2009, MNRAS, 397, 2111
Jones D. H. et al., 2009, MNRAS, 399, 683
Kalberla P. M. W., Burton W. B., Hartmann D., Arnal E. M., Bajaja E., Morras R., Pöppel W. G. L., 2005, A&A, 440, 775
Markevitch M., 1998, A&A, 504, 27
Markevitch M., Vikhlinin A., 2007, Phys. Rep., 443, 1
Nascimento R. S., Ribeiro A. L. B., Trevisan M., Carrasco E. R., Plana H., Dupke R., 2016, MNRAS, 460, 2193
Piffaretti R., Arnaud M., Pratt G. W., Pointecouteau E., Melin J. B., 2011, A&A, 534, A109
Pimbblet K. A., Roseboom I. G., Doyle M. T., 2006, MNRAS, 368, 651
Quintana H., Lawrie D. G., 1982, AJ, 87, 1
Quintana H., Melnick J., Proust D., Infante L., 1996, A&AS, 125, 247
Roettiger K., Loken C., Burns J. O., 1997, ApJS, 109, 307
Shakouri S., Johnston-Hollitt M., Dehghan S., 2016, MNRAS, 458, 3083
Shan H., Qin B., Fort B., Tao C., Wu X., Zhao H., 2010, MNRAS, 406, 1134
Smith G. P., Kneib J., Smail I., Mazzotta P., Ebeling H., Czoske O., 2005, MNRAS, 359, 417
Snowden S. L., Mushotzky R. F., Kuntz K. D., Davis D. S., 2008, A&A, 478, 615
Struble M. F., Rood H. J., 1999, ApJS, 125, 35
Takizawa M., 2000, ApJ, 532, 183
Vijayaraghavan R., Ricker P. M., 2013, MNRAS, 435, 2713
White D. A., Fabian A. C., 1995, MNRAS, 273, 72
Yan P., Yuan Q., Zhang L., Zhou X., 2014, ApJ, 147, 106

APPENDIX

Table A1 lists the member galaxies of A3653.

Table A1. Member galaxies of Abell 3653. The galaxies numbered 19, 22, 28 and 71 are from the 6dF survey.

Number	Object name	RA (J2000)	Dec. (J2000)	Velocity ($km\,s^{-1}$)	Red shift	Magnitude filter
1	GALEXASC J195249.91-520139.6	298.20825	−52.02811	31928	0.1065	17.5R
2	ABELL 3653:PRD 351	298.25292	−52.02064	32587	0.1087	17.7R
3	2MASX J19525707-5202462	298.23787	−52.04611	32887	0.1097	16.2R
4	2MASX J19530336-5202132	298.26404	−52.03700	32947	0.1099	11.2R
5	ABELL 3653:PRD 133	298.27417	−52.02500	32198	0.1074	18.4R
6	ABELL 3653:PRD 347	298.22688	−52.05733	32737	0.1092	17.4R
7	ABELL 3653:PRD 285	298.27729	−52.03906	32947	0.1099	18.1R
8	ABELL 3653:PRD 010	298.18763	−51.99322	31298	0.1044	17.2R
9	ABELL 3653:PRD 349	298.23954	−51.97142	31628	0.1055	17.9R
10	ABELL 3653:PRD 018	298.13488	−52.00225	32108	0.1071	18.1R
11	GALEXASC J195313.18-520313.3	298.30600	−52.05344	32617	0.1088	18.2R
12	ABELL 3653:PRD 050	298.16692	−52.07353	32977	0.1100	18.2R
13	ABELL 3653:PRD 101	298.12083	−52.02139	32258	0.1076	17.7R
14	ABELL 3653:PRD 035	298.10217	−52.04547	30549	0.1019	18.7R
15	GALEXASC J195239.36-520549.8	298.16367	−52.09700	31868	0.1063	17.7R
16	GALEXASC J195306.88-515647.9	298.27804	−51.94678	31478	0.1050	17.1R
17	ABELL 3653:PRD 338	298.12354	−52.08539	31868	0.1063	17.7R
18	ABELL 3653:PRD 245	298.08171	−52.02192	31598	0.1054	17.6R
19	2MASX J19521735-5159465	298.07238	−51.99622	32221	0.1075	16.1b
20	2MASX J19531237-5206322	298.30163	−52.10883	31178	0.1040	16.9R
21	ABELL 3653:PRD 230	298.06113	−52.00808	32198	0.1074	17.8R
22	2MASX J19521995-5205095	298.08312	−52.08589	31604	0.1054	15.9R
23	GALEXASC J195211.95-520042.3	298.04983	−52.01147	29769	0.0993	17.6R
24	ABELL 3653:PRD 029	298.04363	−52.00411	32348	0.1079	17.9R
25	ABELL 3653:PRD 006	298.31296	−51.92744	31298	0.1044	18.7R
26	ABELL 3653:PRD 358	298.38788	−51.97586	32468	0.1083	17.8R
27	GALEXASC J195308.09-515501.9	298.28367	−51.91731	32827	0.1095	18.0R
28	2MASX J19531839-5155491	298.32646	−51.93039	30836	0.1029	16.1R
29	GALEXASC J195209.58-520339.2	298.03967	−52.06108	31658	0.1056	17.3R
30	ABELL 3653:PRD 340	298.14100	−51.91719	32468	0.1083	18.1R
31	ABELL 3653:PRD 057	298.35767	−52.11078	30999	0.1034	17.9R
32	2MASX J19531914-5155201	298.3300	−51.92233	31298	0.1044	16.4R
33	ABELL 3653:PRD 334	298.04671	−51.96708	31178	0.1040	17.9R
34	GALEXASC J195336.19-515744.5	298.39996	−51.96253	30279	0.1010	17.9R
35	ABELL 3653:PRD 198	298.25192	−52.15142	31568	0.1053	18.8R
36	ABELL 3653:PRD 362	298.41796	−52.06881	33727	0.1125	17.8R
37	ABELL 3653:PRD 172	298.01963	−51.98944	31658	0.1056	18.0R
38	ABELL 3653:PRD 049	298.24442	−52.15547	31868	0.1063	18.3R
39	GALEXASC J195326.15-520801.2	298.35921	−52.13342	34386	0.1147	19.1R
40	2MASX J19531989-5154211	298.33308	−51.90594	32917	0.1098	17.0R
41	2MASX J19515849-5203084	297.99375	−52.05239	32767	0.1093	16.2R
42	ABELL 3653:PRD 332	297.99037	−52.00719	31418	0.1048	18.3R
43	ABELL 3653:PRD 007	298.37521	−51.91339	32917	0.1098	18.3R
44	ABELL 3653:PRD 282	298.44896	−52.07464	32737	0.1092	18.0R
45	ABELL 3653:PRD 130	298.39583	−52.13614	31718	0.1058	17.1R
46	ABELL 3653:PRD 364	298.42821	−52.11667	32138	0.1072	17.2R
47	GALEXASC J195304.51-515211.0	298.26929	−51.86925	31928	0.1065	17.4R
48	ABELL 3653:PRD 331	297.97608	−51.96444	32498	0.1084	17.7R
49	2MASX J19530945-5211122	298.28933	−52.18678	33187	0.1107	16.7R
50	ABELL 3653:PRD 090	298.01667	−51.91583	32587	0.1087	17.4R
51	GALEXASC J195254.41-515127.2	298.22683	−51.85711	30699	0.1024	18.5R
52	GALEXASC J195155.56-520639.7	297.98146	−52.11133	32647	0.1089	18.0R
53	ABELL 3653:PRD 279	298.49304	−52.06967	32677	0.1090	18.2R
54	2MASX J19535592-5205196	298.48292	−52.08881	31328	0.1045	16.4R
55	ABELL 3653:PRD 328	297.94571	−51.97167	32348	0.1079	18.4R
56	GALEXASC J195226.88-515104.1	298.11175	−51.85139	30729	0.1025	17.3R
57	ABELL 3653:PRD 093	297.96383	−51.92294	33397	0.1114	18.1R
58	GALEXASC J195139.34-520231.9	297.91392	−52.04194	32887	0.1097	17.2R

Table A1 *– continued*

Number	Object name	RA (J2000)	Dec. (J2000)	Velocity ($km\,s^{-1}$)	Red shift	Magnitude filter
59	ABELL 3653:PRD 066	298.52496	−52.07533	33067	0.1103	17.7R
60	ABELL 3653:PRD 026	297.93000	−51.94375	32917	0.1098	17.6R
61	GALEXASC J195341.68-515207.5	298.42367	−51.86858	33157	0.1106	18.2R
62	ABELL 3653:PRD 121	298.17492	−52.22450	32468	0.1083	18.8R
63	GALEXASC J195412.11-520133.6	298.55071	−52.02583	33157	0.1106	17.6R
64	2MASX J19513315-5202553	297.88796	−52.04878	32198	0.1074	16.9R
65	ABELL 3653:PRD 003	298.53050	−51.93383	30999	0.1034	18.2R
66	2MASX J19532263-5213301	298.34417	−52.22506	32587	0.1087	16.5R
67	GALEXASC J195301.00-514835.7	298.25417	−51.80981	33697	0.1124	17.6R
68	ABELL 3653:PRD 124	298.38650	−52.21856	32318	0.1078	18.5R
69	ABELL 3653:PRD 186	298.36450	−52.22814	32348	0.1079	18.2R
70	ABELL 3653:PRD 325	297.91596	−52.14275	32018	0.1068	18.4R
71	2MASX J19541986-5158230	298.58279	−51.97308	33162	0.1106	15.9R
72	2MASX J19542245-5200250	298.59346	−52.00694	30219	0.1008	16.6R
73	ABELL 3653:PRD 140	298.59604	−52.03164	33847	0.1129	18.1R
74	GALEXASC J195355.47-521137.6	298.48092	−52.19364	33847	0.1129	16.9R
75	ABELL 3653:PRD 031	297.84621	−52.04850	32258	0.1076	17.9R
76	ABELL 3653:PRD 120	298.11296	−52.25203	32108	0.1071	17.9R
77	GALEXASC J195253.38-514642.8	298.22225	−51.77856	31478	0.1050	19.4R
78	ABELL 3653:PRD 080	298.41883	−51.80536	32887	0.1097	17.4R
79	GALEXASC J195117.03-520619.7	297.81967	−52.10514	32378	0.1080	18.7R
80	2MASX J19532972-5216226	298.37396	−52.27300	32767	0.1093	17.0R
81	ABELL 3653:PRD 141	298.65158	−51.99289	31478	0.1050	18.2R
82	ABELL 3653:PRD 181	297.96808	−52.24167	31748	0.1059	18.6R
83	ABELL 3653:PRD 135	298.66808	−52.05789	32498	0.1084	18.0R
84	2MASX J19515019-5148042	297.95904	−51.80125	30609	0.1021	17.4R
85	2MASX J19543069-5209140	298.62792	−52.15383	31838	0.1062	16.5R
86	ABELL 3653:PRD 051	298.34125	−52.29897	32647	0.1089	17.8R
87	ABELL 3653:PRD 187	298.51992	−52.26153	31748	0.1059	18.9R

This paper has been typeset from a TEX/LATEX file prepared by the author.